Mode-III interfacial crack propagation in heterogeneous media

Camille Jestin, Olivier Lengliné, Jean Schmittbuhl

Mode-III interfacial crack propagation in heterogeneous media

Camille Jestin,* Olivier Lengliné, and Jean Schmittbuhl
EOST-IPGS, Université de Strasbourg and Centre National de la Recherche Scientifique, Strasbourg 67084, France

(Received 8 February 2018; published 19 June 2018)

We monitor optically the propagation of a slow interfacial mode III crack along a heterogeneous weak interface and compare it to mode I loading. Pinning and depinning of the front on local toughness asperities within the process zone are the main mechanisms for fracture roughening. Geometrical properties of the fracture fronts are derived in the framework of self-affine scale invariance and Family-Vicsek scaling. We characterize the small and large scale roughness exponents $\zeta_- = 0.6$ and $\zeta_+ = 0.35$, the growth exponent at large scale $\beta_+ = 0.58$, and the power-law exponent of the local velocity distribution of the fracture fronts, $\eta = 2.55$. All these analyzed properties are similar to those previously observed for mode I interfacial fractures. We also observe a common power-law decay of the probability distribution function of avalanche area. We finally observe that amplitude of front fluctuations, local rupture velocity correlation in time, and larger size of events highlight more dynamically unstable behavior of mode III crack ruptures.

DOI: 10.1103/PhysRevE.97.063004

I. INTRODUCTION

Understanding the behavior of crack propagation in heterogeneous materials is of paramount importance both for practical application (e.g., designing more resistant structures [1]) and for its implication in numerous natural science systems (e.g., rock fracture mechanics [2]). Because of this broad repercussion, this topic has attracted considerable interest from the scientific community [3–7]. However, unearthing insights into the local dynamics of the propagating crack remains challenging since direct detailed observations of the running crack are generally not feasible. Most of the time, the fracture evolution is tracked indirectly from remote signals (e.g., acoustic emissions [8–10]). In other instances, the crack analysis is performed through postmortem studies, i.e., once the fracture has extended over the full length of the sample [11–14]. Numerous numerical approaches have also been proposed to model the evolving rupture front [15–19]. However, because of the long-range elastic interactions that are occurring along the crack tip, and the very wide time-scale range (from dynamic rupture processes to long relaxation time scales related to creep processes), numerical simulations require very intensive computation that is not always possible without some significant simplifications.

Some advances about crack propagation in heterogeneous materials have been achieved from experimental setups allowing the direct observation of the crack front growth [12,20,21]. Such setups typically use transparent materials with a weak interface. When the toughness of the interface is much lower than the bulk resistance of the material, an interfacial crack develops over the sample length. This allows the tracking of the location and the geometry of the fracture front from the optical contrast between the attached materials and the open fracture. It is then possible to observe the evolution of quasistatic [6,22,23] or dynamic [24,25] crack propagation. In mode I experiments, the fracture propagates along a plane perpendicular to the applied tensile stress which causes the opening of the two crack surfaces [6]. For these experiments it was found that the crack front has a self-affine scaling invariance with a roughness exponent ζ equal to $\zeta_- = 0.6$ at small scale and a transition to $\zeta_+ = 0.35$ at large scale [26]. This scaling of the front geometry was observed to be independent of the crack front velocity and of the sample surface roughness [20,26]. The dynamic scaling of the fracture fronts that describes the growth of the roughness has been shown to be consistent with a Family-Vicsek scaling [23,27,28]. Another robust property of a slowly propagating mode I crack along heterogeneous interfaces is the distribution of the local velocity of the fracture front. It was shown that, under constant loading velocity, the local velocity fluctuations well obey a power-law distribution above the mean front speed [19,23,29].

There are very few reports of the observation of local front advances of interfacial cracks in heterogeneous media subjected to shear loading modes. This is notably the case for mode III cracks, or antiplane shear cracks where the loading force acts in the plane of the crack propagation but perpendicular to the fracture front propagation direction [6,30]. While it was assumed that all results obtained for the mode I crack can be applied to the shear crack mode, such a hypothesis was mostly based on theoretical arguments and was never experimentally checked [31]. Here we report observations of the local propagation of an interfacial crack under mode I and III loading. The comparison of some relevant features between the two loading modes shows that the microscopical descriptions of both rupture modes are indistinguishable while some differences exist at the macroscale. These observations therefore suggest that the physical process responsible for such features is not dependent on the rupture mode. We focus our observations on the comparisons of the microscopic properties of the crack front propagating in both rupture modes.

*camille.jestin@unistra.fr

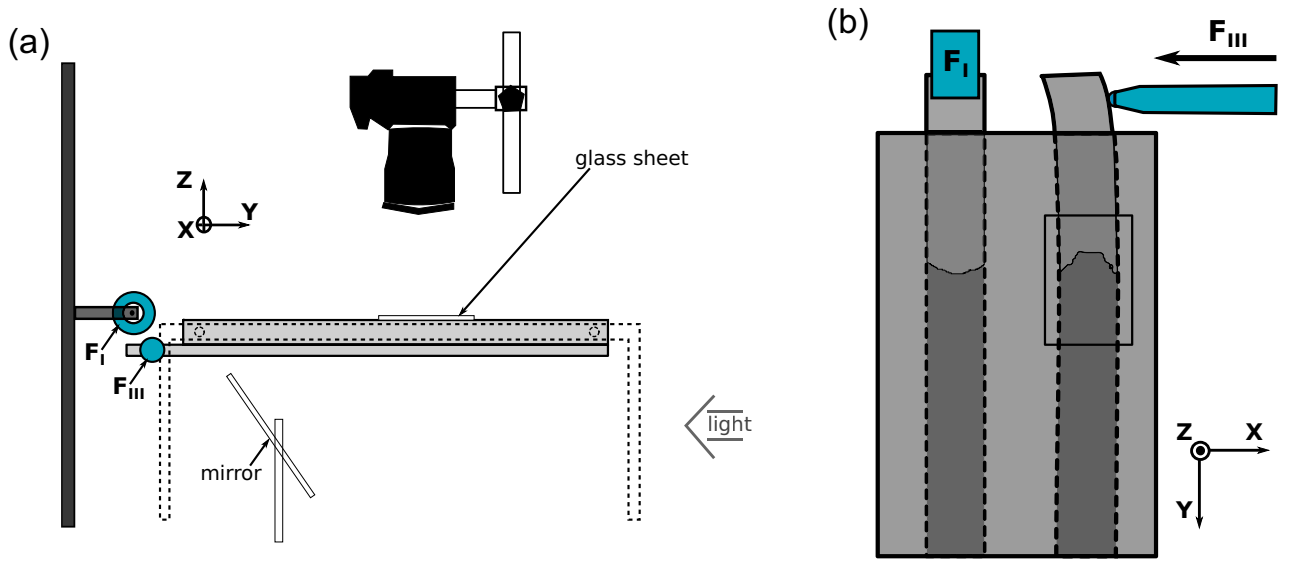

FIG. 1. Experimental setup: (a) side view and (b) top view. F_{I} and F_{III} correspond, respectively, to the mode I and mode III loading forces applied to the narrow plate.

II. METHOD

A. Experimental setup

We follow the same procedure as presented in previous experimental works that led to the observations of interfacial crack mode I features [15,26,31]. The main aspects of the experimental setup are summarized below (for more details, the reader could refer to [20]). We use two transparent polymethylmethacrylate (PMMA) plates of dimension $21 \times 11 \times 0.9$ and $23 \times 2.5 \times 0.5\ \mathrm{cm}^3$ and Young's modulus, $E = 3.2$ GPa. One of the faces of the narrow plate is sand blasted using glass beads of diameter $\phi \in [180; 300]\ \mu$m. We then clean the plate to remove any residual glass beads remaining in the surface. The two plates are assembled by placing the blasted surface of the narrow plate such that it faces the large plate, applying a normal load on the assembly and placing it in an oven at 190 °C for 45 min in order to anneal the plates. This annealing creates a weak cohesive interface with asperities introduced by the sand blasting process. The interface then presents toughness variations, with local fracture energy fluctuating from 18 to $395\ \mathrm{J/m}^2$ [20], but its strength remains lower than the bulk of the material imposing the crack front path to propagate in a plane, i.e., interfacial crack. The wide plate of the sample is then screwed into an aluminium frame as presented in Fig. 1.

Two different motorized translation stages are used in order to apply a mechanical load to the narrow plate. On the one hand, a rolling cylinder applies a force in the z axis at the edge of the narrow plate causing a mode I crack front propagation. The rolling cylinder has a low friction coefficient, therefore limiting the mode II (shear in a direction normal to the fracture front) loading contribution in the present configuration. Because of the current geometry of the experimental setup there still exists a component of mode II loading under such circumstances although this contribution is small compared to the mode I loading [21]. On the other hand, for mode III loading experiments, we use a different translation stage which moves along the x direction. The translation stage is connected to a steel cylinder with a metal bead at its extremity. The metal bead is in contact with the side of the narrow plate at its loose end which then moves along the x direction (Fig. 1). In each experiment the loading point displacement is moving at a constant low speed (on the order of 0.1 mm/s). Both loading modes cause the crack front to advance in a plane in the direction of positive y. We monitor the crack position during its propagation using a Nikon D800 camera. The camera records the advance of the crack front over a typical propagation distance of 1 cm for each experiment at a rate of 2.5 frames per second (fps) and at a resolution of 4800×3200 pixels (pxl). In order to obtain a higher time resolution for some experiments we also use a high speed video camera at 800 fps but with a reduced spatial resolution of 800×600 pxl. After the crack front propagates in the y direction, we stop the displacement of the loading point, and move it back to its initial position such that no loading is applied at the end of the experiment. In order to obtain a high spatial resolution of the crack front morphology we take pictures of it while at rest. This is achieved by mounting the Nikon D800 camera on an optical microscope. Each acquired picture in this configuration has a dimension of 4800×3200 pxl. The microscope and the camera are set on a translation stage that can be moved in order to take neighboring pictures. We take up to 20 adjacent pictures (with some recovery) to obtain a full view of the crack front leading up to a final picture size of $22\,500 \times 8000$ pxl and to a resolution of 0.8 μm/pxl (Fig. 2). The next experiment starts at the location where the previous rupture stopped and so on until the fracture front reaches the extremity of the plate. All experiments have been conducted at room temperature on five different narrow plates, to be sure of the reproducibility of our results. On some occasions we also apply on successive experiments a different loading mode to the same narrow plate in order to guarantee that the observed variations of the crack front that we could observe between mode I loading and mode III loading are actually caused by the loading and not by the sample preparation.

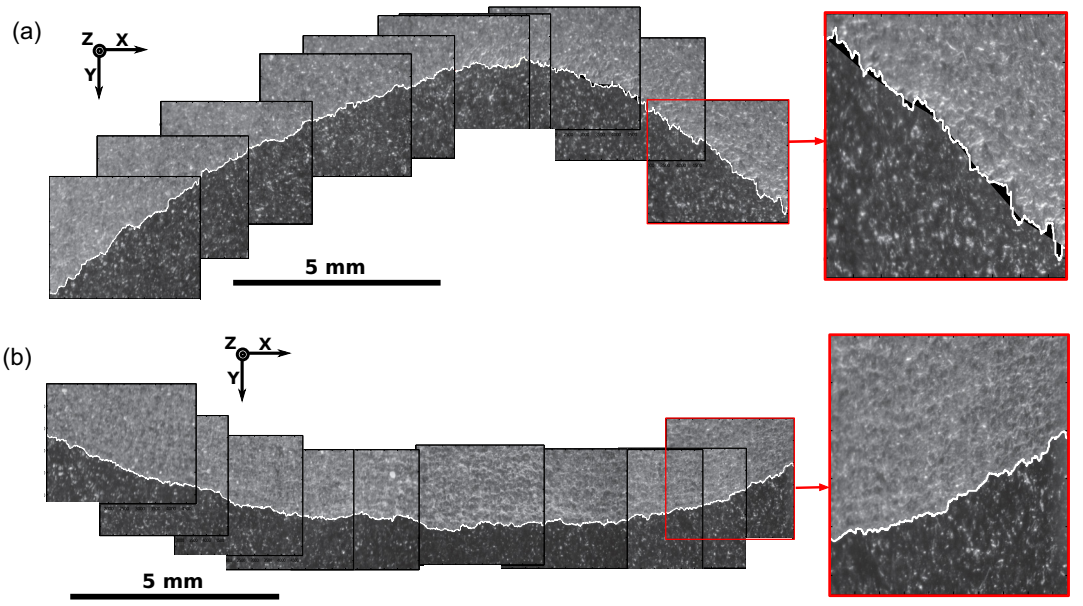

FIG. 2. (a) Mode III crack propagation. (b) Mode I crack propagation. The bright part of the picture represents the already broken area while in the dark zone the sample is still intact (e.g., unbroken). The white line corresponds to the extracted fracture front position $a(x,t)$.

B. Acquisition and image processing

Extraction of front position is achieved by an image processing algorithm consisting of binarizing the crack front pictures so we can differentiate the broken and unbroken parts of the sample. This differentiation is possible because light is transmitted coherently in the cohesive zone while scattered incoherently in the broken part. We use two different methods for the crack front extraction. On the one hand, when crack position is recorded during the crack advance, we proceed with the computation of the difference between grayscale maps of each picture and of the first picture recorded in the experiment. This step enables us to remove any possible permanent artifacts which can appear in our sample. Then, gray figures are converted in black and white using a gray level threshold. We then compute the transition from white to black for each line along the x direction. Finally, we obtain $a(x)$ as the continuous feature marking the transition between the two areas of the pictures. On the other hand, for the high resolution images of the crack front recorded with the microscope and corresponding to the gathering of several pictures, computing picture difference is not possible. In this case, we performed the same processing as described above but without the step of subtracting a reference picture.

III. RESULTS

In the present section, we report on our observations of the fracture front behavior in terms of space and time properties both at large and small scales. We focus our analysis on the possible differences between mode III and mode I loading using mode I as a reference since it has been well examined in previous studies [15,22,23].

A. Self-affinity of the fracture front geometry

We estimate the properties of the front geometry by analyzing 3674 pictures of fronts propagating in mode III (3434 pictures obtained during the crack propagation and 240 acquired using the microscope, when the front is at rest). We do not process, at this stage, the pictures taken by the fast video camera because the associated pictures have a low spatial resolution and thus are not suited for a detailed geometrical analysis. We also used 331 pictures of the crack propagating in mode I (164 obtained during the crack propagation and 167 using the microscope, while the front is at rest). Mode I crack front features have already been widely studied [15,23,32]. Here we redo mode I experiments both to validate our results from the comparison with previous results and also to tease out the possible differences between loading modes.

A readily visible difference between mode III and mode I crack fronts is observed at large scale. Indeed, independently of the used sample or loading velocity, the geometry of the crack front at the sample scale is shown to exhibit a change of curvature which is mode dependent. For a fracture front propagating in mode III, the fracture fronts form a parabola with the vertex located on the loose end side (Fig. 2, top). On the other hand, with a mode I loading, the vertex of the parabola corresponds to the most advanced point of the crack front (Fig. 2, bottom). This large scale geometry difference between these two rupture modes can possibly be attributed to the variation in the stress-intensity factor, $K(x)$. Indeed, in the case of a half-plane crack propagating in an infinite body, large scale stress-intensity factor expression, $K(x)$, has been shown to depend on the considered loading mode [33]. The crack shape variations can then illustrate the large scale changes of K. This change in the large scale front geometry can also be explained by a change in boundary conditions from mode I to mode III configurations. While the mode I experimental setup considers a uniform loading over the whole plate extremity, mode III crack propagation is due to a loading on a single side of the considered narrow plate.

In order to quantify the fluctuations of the crack front positions at smaller scales, we compare the roughness exponent

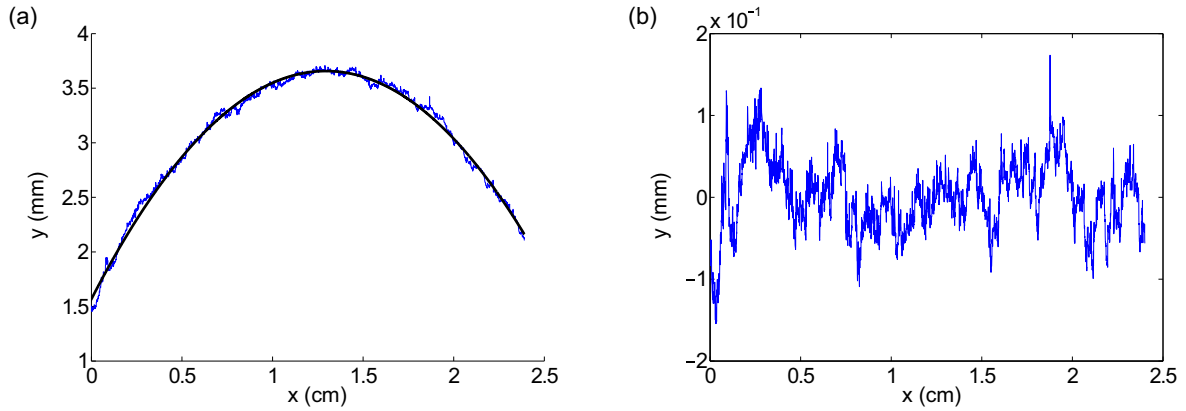

FIG. 3. Example of a geometry obtained for a mode III loading. (a) The thin blue line corresponds to extracted front position and the large black line corresponds to the fitted polynomial of degree 2. (b) Result of substraction of the major trend of the fracture front position.

ζ of the front line $a(x)$ between mode I and mode III. We first remove the large scale trend of the front by fitting $a(x)$ with a polynomial of degree 2 (Fig. 3). We apply a tapering window to the signal, in order to avoid any edge effect that could affect our estimations. This process is achieved for each considered fracture front. We apply two different methods to estimate the roughness exponent which characterizes the self-affine property of the crack front. We first used the power spectrum method [15,22,31] where the Fourier spectrum $P(k)$ of the front position is computed from each of the detrend fronts at all relevant wave numbers k. We then stack all Fourier spectra associated to a given loading mode. We finally get two

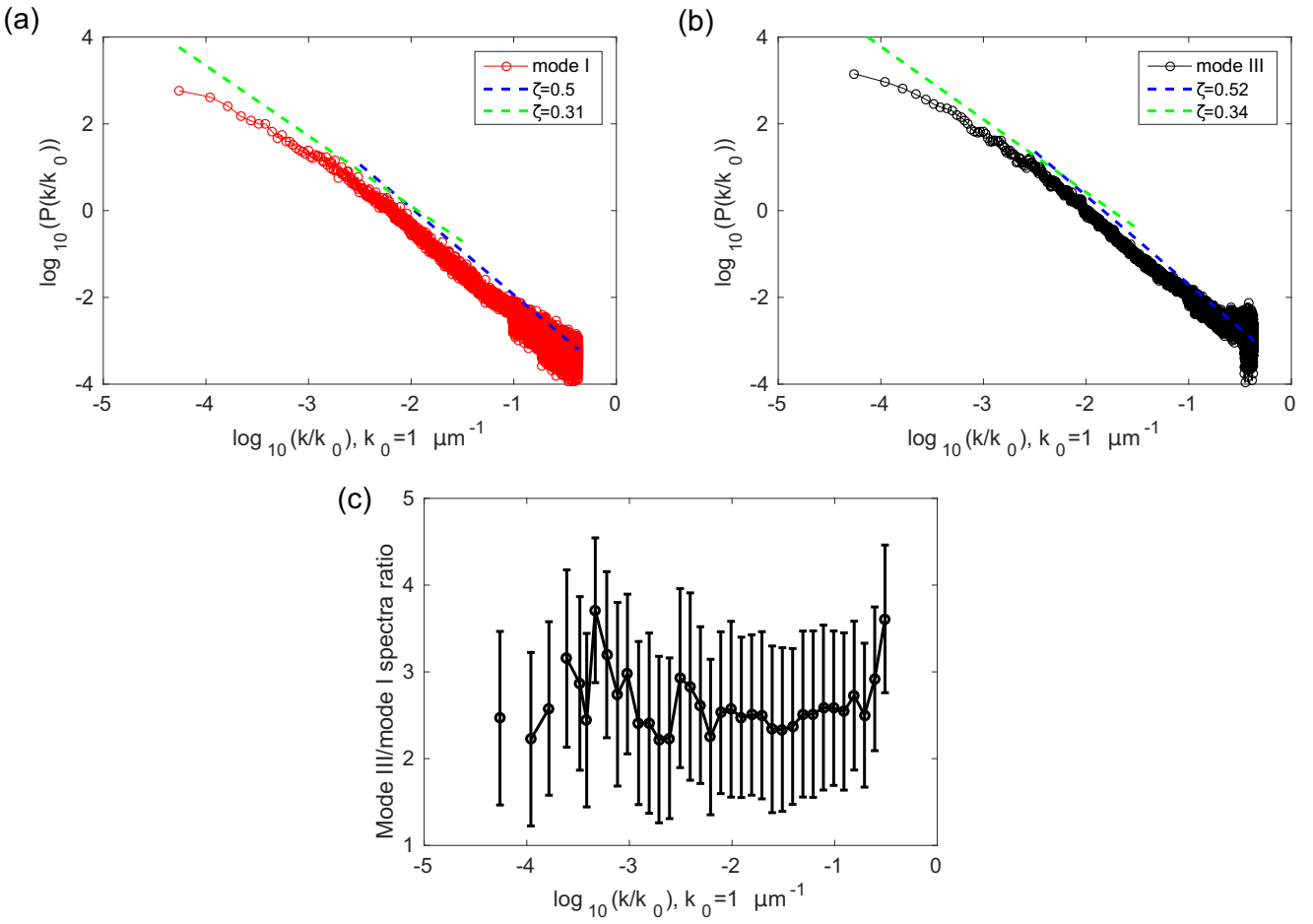

FIG. 4. (a, b) Power spectrum of the crack front. The black line corresponds to mode III loading and the red line corresponds to mode I loading. Green and blue straight lines correspond, respectively, to the representation of Eq. (1) with ζ_+ and ζ_- computed for both loading modes. (c) Ratio between mode III and mode I Fourier spectra.

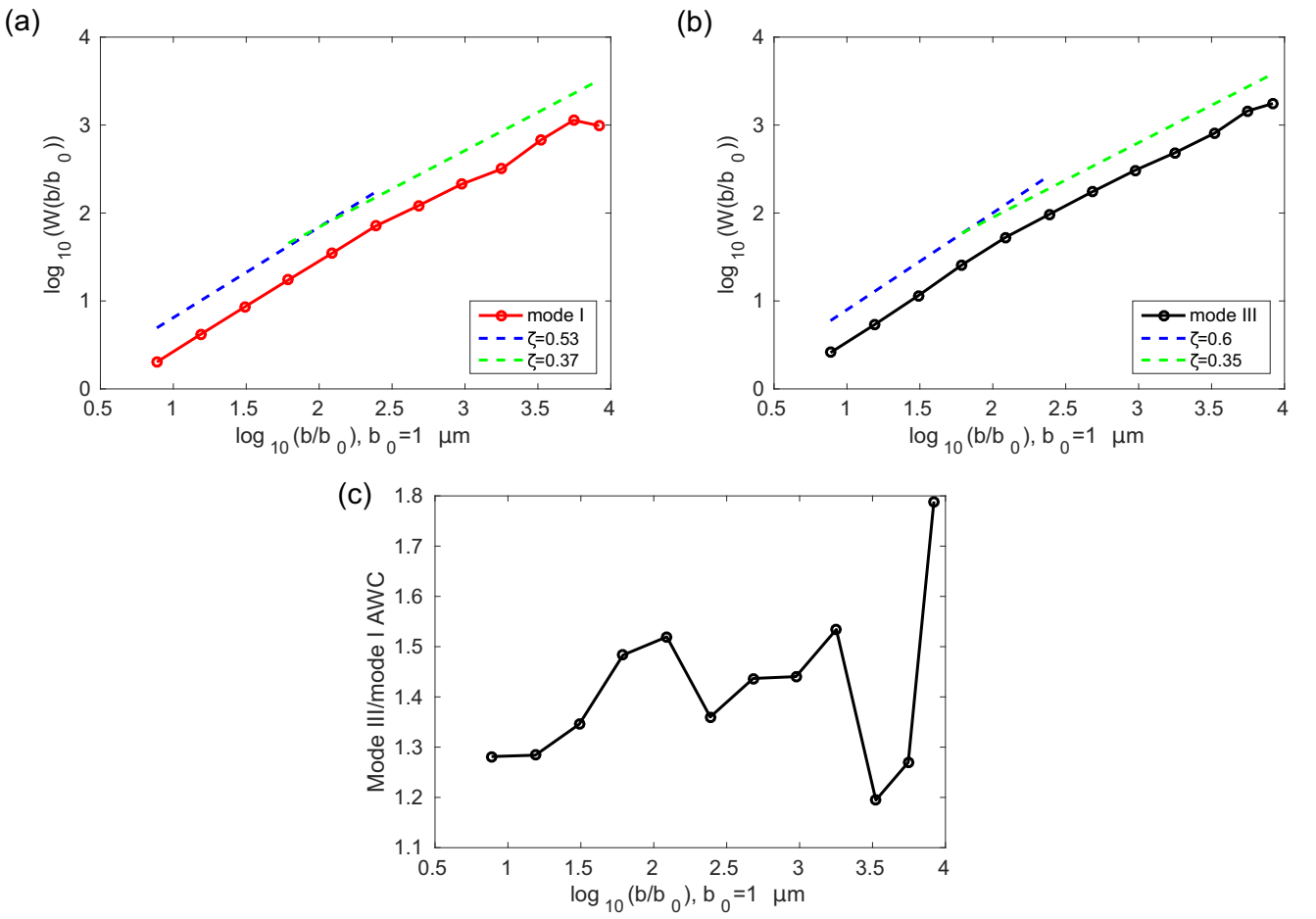

FIG. 5. (a, b) Averaged wavelet coefficient. The black line corresponds to mode III loading and the red line corresponds to mode I loading. Green and blue lines represent, respectively, the power law of Eq. (2) with ζ_+ and ζ_- defined in the legend. (c) Ratio between mode III and mode I averaged wavelet coefficients.

spectra that are representative of each of the two loading modes (Fig. 4). We observed that both spectra have the same shape and slope. In order to quantify the roughness exponent attached with each mode, we fit the power spectrum, $P(k)$, by

$$P(k) \propto k^{-1-2\zeta}, \tag{1}$$

where ζ is the roughness exponent. We observe in Fig. 4 two different scaling regimes. The first one at large scale (i.e., small k), below $k^* = 100\ \mu\text{m}^{-1}$, shows a self-affine behavior with a roughness exponent equal to $\zeta_+ = 0.31 \pm 0.1$ for mode I crack propagation and $\zeta_+ = 0.34 \pm 0.1$ for mode III. At small scale, above $k^* = 100\ \mu\text{m}^{-1}$, we find the same roughness coefficient values equal to $\zeta_- = 0.5 \pm 0.1$ and 0.52 ± 0.1 for mode I and mode III, respectively. Uncertainties on the roughness exponents are deduced from the least square fitting of the power spectra.

We obtain from this method very close values of ζ for both mode I and mode III loadings. Results are in accordance with the observations made in previous studies [19,26], where the roughness exponent has been shown to exhibit a transition from 0.6 to 0.35 going from small to large scale (Fig. 4). Moreover, the cross-over length k^* is also in agreement with the values reported in [26]. In order to detect if any difference in cross-over length values exists between the two studied loading modes, we compute the ratio $P(k)$ obtained in loading mode I and mode III (Fig. 4, bottom). We cannot detect any obvious deviation of this ratio that would reflect a change of cross-over length scale. Figure 4 (bottom) shows, however, a clear difference between mode I and mode III spectra in terms of amplitude, the mode III spectrum having a magnification factor $\delta \sim 2.5$.

In order to confirm our roughness exponent assessment, we used a second method: the averaged wavelet coefficient (AWC) [26,28,31], which consists of the transformation of the front position in the wavelet domain. The averaged wavelet coefficients $W[h](b)$ are obtained as a function of the scale parameter b. The averaged wavelet coefficients enable an estimate of the roughness exponent ζ using results presented in Fig. 5 and the relationship

$$W[h](b) \propto b^{1/2+\zeta}. \tag{2}$$

Figure 5 reveals similar results for mode I ($\zeta_+ \sim 0.37 \pm 0.1$ and $\zeta_- = 0.53 \pm 0.1$) and mode III ($\zeta_+ \sim 0.35 \pm 0.1$ and $\zeta_- = 0.60 \pm 0.1$) crack front propagation. These results confirm the existence of two roughness exponents and a cross-over wavelet coefficient $b^* = 100\ \mu\text{m}$ between the two regimes. Figure 5 (bottom) also confirms that there are no noticeable differences between mode I and mode III loading. We notice again a larger

amplitude for mode III crack propagation with a magnification factor $\delta \sim 1.5$.

In this paper, the use of a small pixel size enables access to the small scale regime. However, the image resolution can also have an impact on roughness exponent estimates. Indeed, in the Appendix, we demonstrate that lowering the dynamic range of the signal, $a(x)$, can impact the scaling properties analysis at small scale. We show that, as this dynamic range decreases, the roughness exponent values at small scale deviate from the original scaling. However, we demonstrate that the range used in our experiments is sufficient to recover the scaling exponent (see the Appendix).

B. Dynamic properties of the fracture front

We now turn to the estimation of the differences in the time evolution between mode I and mode III configurations. During the different conducted experiments, we observed various fracture dynamics. Although mode I crack propagation is systematically stable, mode III fracture propagation seems to be more complex. Half of the experiments conducted under mode III loading were unstable. In these cases, after a propagation of a few millimeters, the crack advances a typical distance of ~1 cm in less than 0.1 s. This fast propagation makes us unable to capture the front position during these fast stages, even using the fast camera. Instability of the front is observed over the whole sample length in a subset of experiments related to two specific narrow plates. However, in the other half of the experiments conducted with a mode III loading, the front propagates slowly (~0.15 mm/s), without high crack speed fluctuations at large scale. When the evolution of the fracture position with time was sufficiently slow to be acquired, we analyzed all the pictures obtained while the front was propagating. The crack front propagation is sampled every 0.04 to 0.4 s with a resolution from 5.2 to 13 μm/pxl. For each experiment we record from 40 to 850 pictures for a crack propagating within 1-cm advance. As the fracture front propagates through the interface, the rupture front is actually roughening owing to the pinning and depinning of the front on toughness asperities. This process was quantified by considering the difference a_m between front position at time t and the fracture front at time t_0 [23,27]:

$$a_m(x,t) = a(x,t) - a(x,t_0). \tag{3}$$

The growth of the width of the fracture front can then be described using the root mean square σ of the function a_m [23,35]:

$$\sigma(t) = \sqrt{\langle a_m(x,t)^2\rangle_x - \langle a_m(x,t)\rangle_x^2} \tag{4}$$

where $\langle X\rangle_x$ is used to describe the average value of X over x. We compute $\sigma(t)$ for each experiment and stack the evolution of σ for each loading mode (Fig. 6) assuming that the average position of the front $\bar{a}$ is proportional to time. We observe a power-law growth of the fracture front roughness with time as $\sigma \propto \bar{a}^{\beta_+}$ both for mode I and mode III. Moreover, propagations under both loading modes are in very good agreement with the prediction of Stormo *et al.* [19] of an exponent $\beta_+ = 0.58$. Actually, this scaling is deduced from a Family-Vicsek scaling

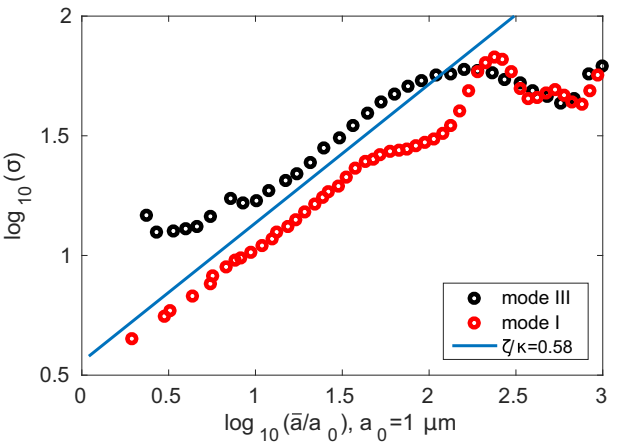

FIG. 6. Standard deviation of the width of the fracture as a function of the average front position $\bar{a}$. Red and black dots correspond, respectively, to mode I and mode III fracture propagation. The blue line is a power law with the growth exponent $\beta_+ = 0.58$ associated to a Family-Vicsek scaling where $\zeta_+ = 0.35$ and $\kappa_+ = 0.6$.

[27,34,35]:

$$\sigma(t,L) \propto L^{\zeta}\phi\left(\frac{\bar{a}}{L^{\kappa}}\right), \tag{5}$$

with $\bar{a}$ the average position of the fracture front position and $\phi(x)$ the scaling function defined by

$$\phi(x) = \begin{cases} x^{\zeta/\kappa} & x \to 0 \\ \text{const} & x \to \infty \end{cases} \tag{6}$$

where $\zeta/\kappa = \beta$ is the growth exponent. $\beta_+ = 0.58$ is consistent with previously numerically measured $\zeta_+ = 0.35$ and $\kappa_+ = 0.6$ [19].

C. Local crack velocity distribution

An other comparison between the two sets of experiments (mode I and mode III loading) is performed from the distribution of the local crack front velocities. Such a distribution was shown to be very reproducible over various average crack velocities during mode I crack propagation. The velocity distribution is computed using the waiting time matrix (WTM) [29], which gives the time spent by the crack front in each pixel of the image. To compute this matrix, we represent the front lines $a(x,t)$ using a matrix form as $A(x,a(x,t)) = 1$ at the front position and zero elsewhere considering the matrix size equal to the image size [32]. The WTM is defined as the sum of front matrices A:

$$W(x,y) = \sum_t A(x,a(x,t)). \tag{7}$$

It is a matrix of integers. To get the physical waiting time matrix, we multiply each matrix element W by the time step δt. From this WTM, we compute the local velocity matrix as $V(x,y) = p/w(x,y)$, with p the pixel size. From $V(x,y)$, we deduce the local velocity along each front $a(x,t)$ and build the spatiotemporal velocity matrix $v(x,t) = V(x,a(x,t))$. From the velocity matrices computed for 18 experiments (six in mode I loading conditions and 12 in mode III), we evaluate the

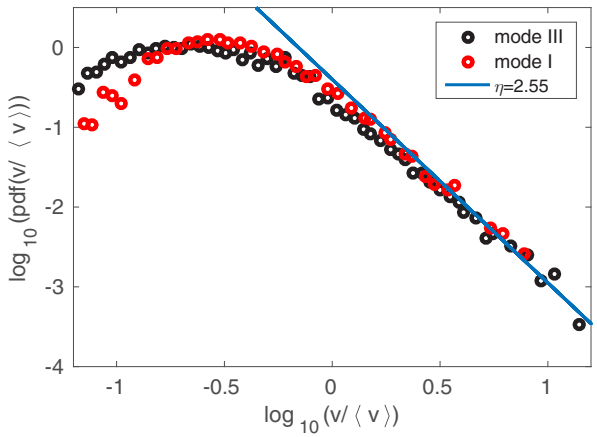

FIG. 7. Local velocity distributions for mode I (red dots) and mode III (black dots) deformations. The blue line represents the power law $P(v/\langle v\rangle) \propto (v/\langle v\rangle)^{-\eta}$ with $\eta = 2.55$.

normalized probability density function (pdf) $P(v/\langle v\rangle)$, with $\langle v\rangle$ the average front velocity of the considered experiment. We finally collapse the results of all experiments with a similar loading mode (Fig. 7). The distributions for each loading mode appear very similar with no significant deviation between each other. In particular, we find that the scaling of P at speed higher than the average speed follows the trend already observed for mode I fracture:

$$P(v/\langle v\rangle) \propto \left(\frac{v}{\langle v\rangle}\right)^{-\eta} \quad \text{for} \quad \frac{v}{\langle v\rangle} > 1, \tag{8}$$

with the exponent $\eta \sim 2.55$. This therefore suggests that the shape of local velocity distribution is not affected by the loading condition imposed on the system.

D. Space and time correlations

The power-law distributions of the local velocities, for both loading modes I and III, indicate the presence of intermittent local activities of the front with depinning transition at high velocity. In order to characterize the local dynamics of the crack front propagation, we study the space and time correlation of local velocities. We define the autocorrelation functions in space, $G(\Delta x)$, and time, $G(\Delta t)$, for the local velocities $v(t,x)$, as [32]

$$G(\Delta x) = \left\langle \frac{\langle [v(x+\Delta x,t) - \langle v\rangle_x][v(x,t) - \langle v\rangle_x]\rangle_x}{\sigma_x^2} \right\rangle_t, \tag{9}$$

$$G(\Delta t) = \left\langle \frac{\langle [v(x,t+\Delta t) - \langle v\rangle_t][v(x,t) - \langle v\rangle_t]\rangle_t}{\sigma_t^2} \right\rangle_x \tag{10}$$

with $\langle v\rangle_x$ and $\langle v\rangle_t$, respectively, the spatial and temporal average of the velocity, and σ_x and σ_t the spatial and temporal standard deviations.

Autocorrelation functions are computed for crack fronts propagating in mode I and III. Fracture front position is monitored using the fast camera, with a sampling rate equal to 800 images per second and a resolution of 25 μm/pxl. Results are represented in Fig.8. Data have been fitted with power-law functions combined with an exponential cutoff such as

$$G(\Delta x) \propto \Delta x^{-\chi} \exp(-\Delta x/x^*), \tag{11}$$

$$G(\Delta t) \propto \Delta t^{-\tau} \exp(-\Delta t/t^*), \tag{12}$$

where χ and τ are the average exponents and x^* and t^* are the average cutoff or correlation lengths, respectively, for space and time correlations. Values of these parameters are reported in Table I.

Though results on average exponents that we compute are slightly lower than those obtained in [32], we find comparable values of average cutoff both in space and time. Average exponents obtained for experiments conducted in mode I and mode III are similar. Yet, we observe, for mode III loading, higher mean values, t^* and x^*, than those obtained for mode I. This then seems to confirm that mode III loading leads to more unstable crack front propagation than in mode I.

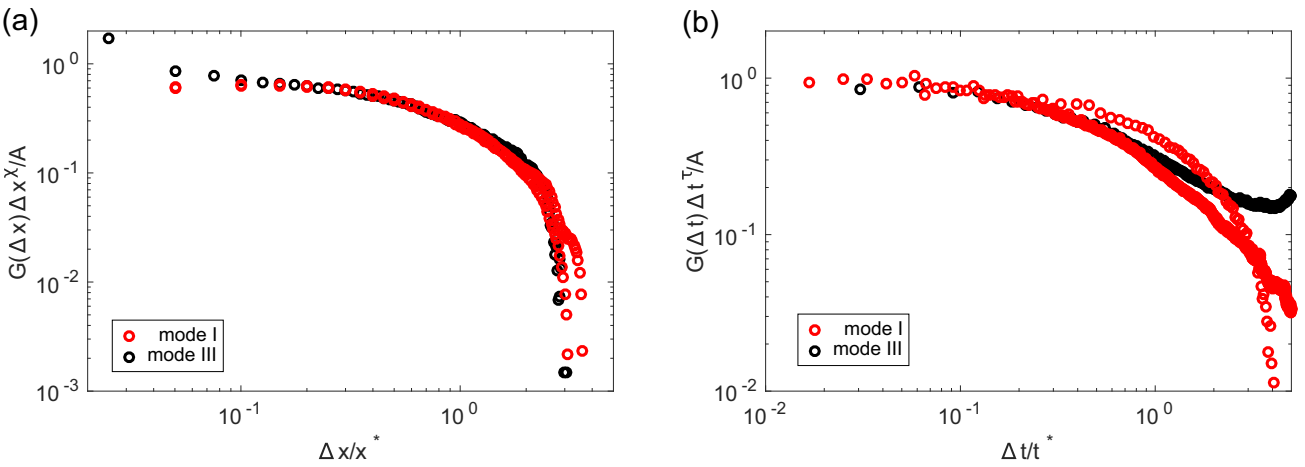

FIG. 8. Space correlation functions (a) and time correlation functions (b) for mode I (red) and mode III (black) crack propagation. Functions have been collapsed onto one another according to the power laws with exponential cutoff. For spatial correlation, $G(\Delta x) = A\Delta x^{-\chi} \exp(-\Delta x/x^*)$, and, for temporal correlation, $G(\Delta t) = A\Delta t^{-\tau} \exp(-\Delta t/t^*)$.

TABLE I. Results of computed values of average cutoff describing autocorrelation functions in space and time [Eqs. (11) and (12)].

	y^* ($t^* = y^*/\langle v \rangle$)	τ	x^*	χ
Mode III	$50 \pm 5\,\mu$m	0.1	$1000 \pm 100\,\mu$m	0.28
Mode I	$14 \pm 5\,\mu$m	0.1 ± 0.05	$450 \pm 50\,\mu$m	0.3
Mode I [32]	$7\,\mu$m	0.43	[92,131] μm	0.53 ± 0.12

E. Avalanches' size distribution

We are interested, in this section, in the size distribution of avalanches generated by the depinning of the fracture front. We use experiment results recorded by the fast camera. We define avalanches as the areas where the front propagates with a velocity $v \geqslant C\langle v \rangle$, with $\langle v \rangle$ the average local velocity and $C = 10$ [36], and we obtain a catalog of rupture areas S in number of pixels. We compute the distribution of these areas, pdf(S) (see Fig. 9), for both mode I and mode III loadings. Size distributions are very similar, following a power law: $\text{pdf}(S) \propto S^{-\gamma}$, with $\gamma = 1.8 \pm 0.1$ for $S < 10^{2.5}$. This value of γ is comparable to results obtained in previous studies [29,32,36]. We also observe larger events for mode III loading than for mode I.

IV. DISCUSSION

Lengliné *et al.* [21] have proposed that a mode II contribution (i.e., a shear in a direction normal to the crack front [6]) is present during the crack propagation under the tensile force loading of the current setup. Because of the current geometrical configuration of the sample, a mode II component is introduced at the crack tip. Lengliné *et al.* [21] showed that under the same configuration used in our experiments the ratio $G_{\text{II}}/G_{\text{I}}$ is close to 15% when the plate is loaded by the tensile force perpendicular to the plate interface and where G_α refers to the energy release rate related to the loading mode α. Under our mode III loading, when the force acts parallel to the plane of crack propagation, our experimental setup is very similar to the split cantilever beam (SCB) test. For such a fracture propagation, it was tested numerically that a mode II component is also present at the crack tip while the mode I component is negligible. Overall, it has been shown that the mode II component in the SCB specimen is around 40% of the total energy release rate [37]. However, it is noted that the mode II component is the most significant at the free edges of the crack and is zero at the middle of the crack. On our analyzed pictures, the portions at the edges of the crack are not taken into account. This further reduces the importance of the mode II component in the analyzed results. Then, although a mode II component is present at the crack tip under both loading conditions in our experiments, this component remains much lower than the respective mode I or mode III loading.

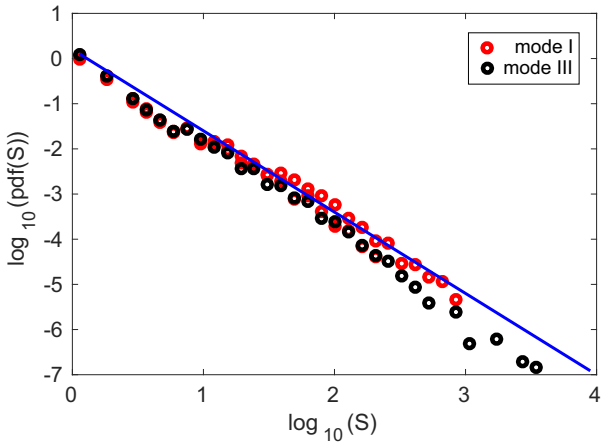

FIG. 9. Probability distribution of pinning size for mode I (red circles) and mode III (black circles) crack propagations. The blue line represents the power law $\text{pdf}(S) \propto S^{-\gamma}$, with $\gamma = 1.8$.

Although the observation of some differences at large scale, such as general front shape and instabilities during the crack propagation, the small scale geometrical and dynamical properties of the slow propagating antiplane (mode III) cracks along our heterogeneous interface are not significantly affected by the loading mode. All the tested features (roughness exponents, dynamical exponents, local velocity distribution, and avalanche size distribution) are similar to those obtained for mode I cracks. Numerous models have been previously proposed to explain the mode I crack propagation and notably the associated roughness exponents characterizing the crack front geometry. In particular the elastic line model which relies on a first order derivation of the stress intensity factor has been widely studied at large scales [4,38]. In this model, when the deviation of the crack front from a straight line is small, the stress intensity factor, K, at the crack tip can be expressed as a function of the front geometry. Then the perturbation equation is given by

$$K(x) = K^0[a(x)]\left(1 + \frac{M_\alpha}{2\pi} PV \int_{-\infty}^{+\infty} \frac{da(x')/dx'}{x' - x} dx'\right) \tag{13}$$

and the coefficient M_α is

$$M_{\text{I}} = 1, \tag{14}$$

$$M_{\text{II}} = \frac{2 - 3\nu}{2 - \nu}, \tag{15}$$

$$M_{\text{III}} = \frac{2 + \nu}{2 - \nu}, \tag{16}$$

depending on the crack mode [31,38]. We readily observe from Eq. (13) that the difference between mode I and mode III only arises through the constant term M and depends only on the Poisson's ratio ν. If the strength of the interface and its associated statistical properties (spatial distribution and length correlation) are the same for both mode I and mode III cracks (which is the case in our experiments), and assuming that the front is propagating locally when the stress intensity factor reaches the local strength, then we expect a similar microscopic description of the geometry of the crack front geometry. This therefore supports the similar shape and local dynamic properties of mode I and mode III interfacial cracks. A significant limitation of this model, however, is that the dynamic exponent of crack fronts simulated within this framework is limited to the large scale exponent ($\zeta_+ = 0.35$) different from the low scale exponent ($\zeta_- = 0.6$). On the other hand, in the soft clamp fiber bundle model [19,39], both

exponents are predicted. In this kind of model the breakage of any local sites of the interface is controlled by elastic force redistribution not only along the crack front as stated in Eq. (13) but also in the process zone ahead of the front. This can occur because the stress intensity factor ahead of the crack may locally exceed the strength threshold of the interface in the process zone. For both rupture modes, the decay of the stress, σ_{zz} or σ_{zx}, as a function of the distance from the crack tip is following the same scaling as $\sigma \propto 1/\sqrt{r}$. Numerical simulations performed in respect of this kind of model predict that the roughness exponent describing the front geometry at small scale is close to the experimental value $\zeta = 0.6$. Supposing that the spring elongation stiffness used in [19] can be represented by a shear stiffness and using the same dependence of $\sigma \propto 1/\sqrt{r}$, we are expecting, for our model, similar results for mode I and mode III cracks. In this sense, the two scaling regimes of the crack front geometry, at both small and large scale, can be linked to two mechanisms (the elastic line model at large scale and damaged percolation at small scale) that behave independently of the loading mode. For mode I fracture propagation, the transition scale between small and large scale regimes has been shown to be related to the stiffness ratio of the bulk material and the interface [19]. A similar ratio is expected to exist in the mode III configuration. These arguments promote the similarity of the crack geometry features observed for mode I and mode III cracks.

However, a noticeable difference between the two modes is observed on the prefactor of the various observed scaling (Fourier spectra, wavelet coefficients, and Family-Vicsek). Indeed we always observe that mode III cracks have higher amplitude of the front fluctuations compared to their mode I counterparts. Interestingly, we see from Eq. (13) that M_{III} is larger than M_{I}. Knowing that Poisson's coefficient is on the order of $\nu = 0.4$ for PMMA [40], it leads to a ratio $M_{\mathrm{III}}/M_{\mathrm{I}} = 1.5$ which is on the order of the amplitude ratio of the front fluctuations. Moreover, higher fluctuations of the stress intensity factor in mode III configuration imply that the stress distribution at the crack tip is consequently more heterogeneous. This might be an explanation for the more unstable nature of the mode III crack as the shear stress [as derived from Eq. (13)] can become locally high and leads to larger dynamic events. This is confirmed by the observation of a longer decay in the time correlation of local velocities and the presence of larger event sizes during the crack propagation.

V. CONCLUSION

We have studied experimentally the behavior of a crack propagating along a heterogeneous interface. We compared the details of the rupture pinning and depinning for loading modes I and III. The roughness exponent, for both of these modes, has been shown to be $\zeta_- \sim 0.6$ at small scale and $\zeta_+ \sim 0.35$ at large scale, in accordance with previous mode I loading studies that used the same experimental setup [22,23,31]. The growth exponent is shown to be similar between both modes, $\beta_+ = 0.58$, very consistent with numerical simulations [19]. We also observed similar results for the probability distribution of local crack velocities for mode I and mode III. Thus, conclusions made in previous theoretical studies, stating that observations made in mode I can be extended for mode III [31], seem to be verified. This paper therefore highlights the importance of local pinning and depinning processes in controlling the rupture propagation in heterogeneous media.

ACKNOWLEDGMENTS

This research is conducted in the framework of the Labex G-EAU-THERMIE (Investissements d'Avenir). We are very grateful to Alain Steyer for his technical support. We thank the reviewers for their comments and questions on our paper. Finally, we thank Mike Heap for grammatical assistance.

APPENDIX: INFLUENCE OF PIXEL SIZE ON ROUGHNESS EXPONENT ESTIMATES

We use, for roughness exponent estimates, two different pixel sizes. The first one is related to pictures of size 4800 ×

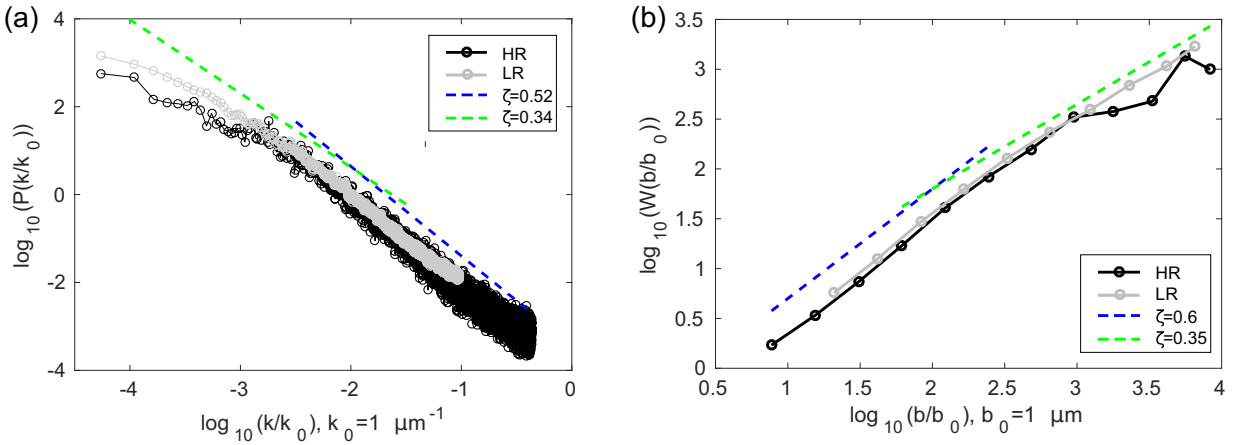

FIG. 10. (a) Average power spectrum of crack fronts obtained from pictures recorded with the combination of microscope and Nikon D800 camera (black, high resolution, HR) and with the camera only (gray, lower resolution, LR). (b) Average wavelet coefficient of crack fronts obtained from pictures recorded with the combination of microscope and Nikon D800 camera (black) and with the camera only (gray).

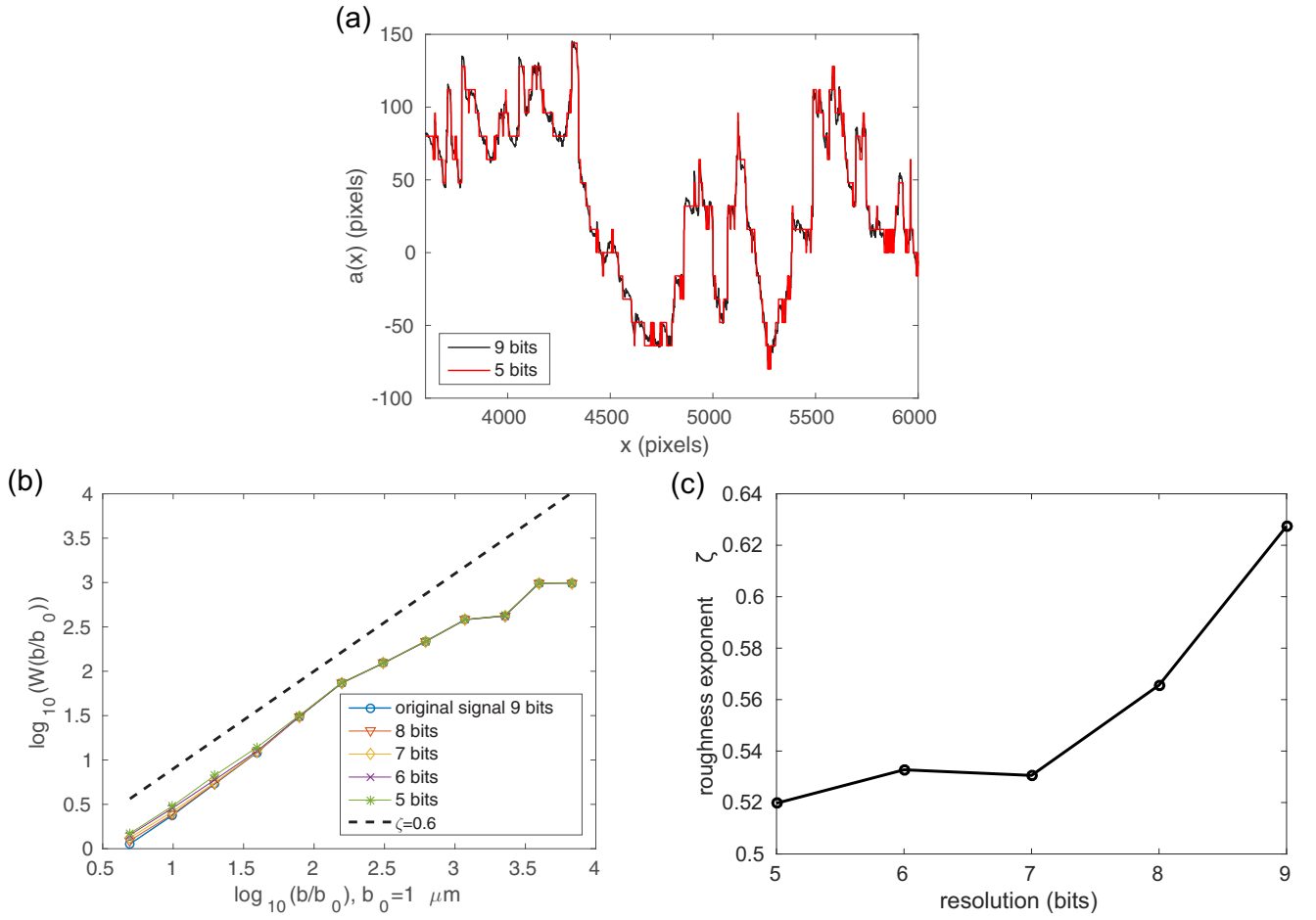

FIG. 11. (a) Fracture front position with two different resolutions: the original resolution of 9 bits and a 5-bit resolution for the local height $a(x)$. (b) Scaling using the average wavelet coefficient method applied to the same front filtered at different resolutions: 5, 6, 7, 8, and 9 bits. (c) Roughness exponent values computed at small scale ($b/b_0 < 2$, $b_0 = 1$ μm) for different crack front resolutions.

3200 pxl obtained with the Nikon D800 camera. For this case, the pixel size is equal to 5 μm/pxl. The second one is related to pictures obtained with the combination of a microscope and the Nikon D800 camera. For this configuration, the pixel size is equal to 1 μm/pxl. In Fig. 10 are represented two averages of the power spectrum and average wavelet coefficients over two different sets of images of the crack front. The first set (red) corresponds to the first configuration (camera only), and the second set (blue) corresponds to the second configuration (camera and microscope). We can see that, in the common range of wavelengths, the spectra superimpose. We note that the use of a smaller pixel size enables one to track higher wave numbers. This is important for (i) estimating over the largest possible range of length scales the roughness exponent at small scale and (ii) characterizing the wave number k^* at which the transition occurs between the two regimes. In our experiments the decrease of pixel size does not seem to affect the roughness exponent measurement and appears to be sufficient for a correct estimate of k^*.

Moreover, in order to test more precisely the impact of these differences in pixel size on the roughness exponent, we follow the work presented by Delaplace *et al.* [41]. We numerically decrease the resolution for the front position $a(x)$ as presented in Fig. 11, top. This resolution decrease is achieved by lowering the dynamic range of the signal, $a(x)$. We numerically reduce the original resolution, $\log_2\{\max[a(x)] - \min[a(x)]\} = 9$ bits, with $a(x)$ in pixels, to obtain four new signals with $\log_2\{\max[a(x)] - \min[a(x)]\} = 5$, 6, 7, and 8 bits. Figure 11, top, shows the same signal $a(x)$ with two different resolutions: 5 and 9 bits. We analyze the scaling properties of each computed new signal using the average wavelet coefficient method (Fig. 11, bottom left). As the dynamic range decreases, we observe, at small scale, a significant deviation of the average wavelet coefficient from the original scaling. Figure 11, bottom right, represents the roughness exponent computed at small scale ($b/b_0 < 2$, $b_0 = 1$ μm) for each resolution. This figure confirms that the dynamic range in pixels used for our paper is sufficient to recover the scaling exponent of the front at small scale.

[1] J. R. Rice, in *Mathematical Analysis in the Mechanics of Fracture*, edited by H. Liebowitz (Academic Press, New York, 1968), Vol. 2.

[2] C. H. Scholz, Earthquakes and friction laws, Nature (London) **391**, 37 (1998).

[3] B. B. Mandelbrot, D. E. Passoja, and A. J. Paullay, Fractal character of fracture surfaces of metals, Nature (London) **308**, 721 (1984).

[4] H. Gao and J. R. Rice, Shear stress intensity factors for a planar crack with slightly curved front, J. Appl. Mech. **53**, 774 (1986).

[5] M. J. Alava, P. Nukala, and S. Zapperi, Statistical models of fracture, Adv. Phys. **55**, 349 (2006).

[6] D. Bonamy and E. Bouchaud, Failure of heterogeneous materials: A dynamic phase transition? Phys. Rep. **498**, 1 (2011).

[7] A. Hansen, P. C. Hemmer, and S. Pradhan, *The Fiber Bundle Model: Modeling Failure in Materials* (Wiley, New York, 2015).

[8] E. J. Sellers, M. O. Kataka, and L. M. Linzer, Source parameters of acoustic emission events and scaling with mining-induced seismicity, J. Geophys. Res. **108**, 1 (2003).

[9] B. D. Thompson, R. P. Young, and D. A. Lockner, Premonitory acoustic emissions and stick-slip in natural and smooth-faulted Westerly granite, J. Geophys. Res. **114**, B02205 (2009).

[10] Y. Mo, S. A. Greenhalgh, J. O. A. Robertsson, and H. Karaman, The development and testing of a 2D laboratory seismic modelling system for heterogeneous structure investigations, J. Applied Geophys. **116**, 224 (2015).

[11] A. K. Maji and J. L. Wang, Experimental study of fracture processes in rock, Rock Mech. Rock Eng. **25**, 25 (1992).

[12] J. Schmittbuhl, F. Schmitt, and C. Scholz, Scaling invariance of crack surfaces, J. Geophys. Res.: Solid Earth **100**, 5953 (1995).

[13] M. J. Heap, P. Baud, P. G. Meredith, A. F. Bell, and I. G. Main, Time-dependent brittle creep in darley dale sandstone, J. Geophys. Res. **114**, 1 (2009).

[14] J.-B. Kopp, J. Schmittbuhl, O. Noel, J. Lin, and C. Fond, Fluctuations of the dynamic fracture energy values related to the amount of created fracture surface, Eng. Fract. Mech. **126**, 178 (2014).

[15] J. Schmittbuhl, S. Roux, J.-P. Vilotte, and K. J. Måløy, Interfacial Crack Pinning: Effect of Nonlocal Interactions, Phys. Rev. Lett. **74**, 1787 (1995).

[16] E. Bouchaud, Scaling properties of cracks, J. Phys.: Condens. Matter **9**, 4319 (1997).

[17] H. Perfettini, J. Schmittbuhl, and J.-P. Vilotte, Slip correlations on a creeping fault, Geophys. Res. Lett. **28**, 2137 (2001).

[18] M. Adda-Bedia, E. Katzav, and D. Vandembroucq, Second-order variation in elastic fields of a tensile planar crack with a curved front, Phys. Rev. E **73**, 035106 (2006).

[19] A. Stormo, O. Lengliné, J. Schmittbuhl, and A. Hansen, Soft-clamp fiber bundle model and interfacial crack propagation: Comparison using a non-linear imposed displacement, Front. Phys. **4**, 1 (2016).

[20] O. Lengliné, J. Schmittbuhl, J. E. Elkhoury, J.-P. Ampuero, R. Toussaint, and K. J. Måløy, Downscaling of fracture energy during brittle creep experiments, J. Geophys. Res. **116**, B08215 (2011).

[21] O. Lengliné, R. Toussaint, J. Schmittbuhl, J. E. Elkhoury, J.-P. Ampuero, K. T. Tallaskad, S. Santucci, and K. J. Måløy, Average crack-front velocity during subcritical fracture propagation in a heterogeneous medium, Phys. Rev. E **84**, 036104 (2011).

[22] J. Schmittbuhl and K. J. Måløy, Direct Observation of a Self-Affine Crack Propagation, Phys. Rev. Lett. **78**, 3888 (1997).

[23] K. J. Måløy and J. Schmittbuhl, Dynamical Events During Slow Crack Propagation, Phys. Rev. Lett. **87**, 105502 (2001).

[24] J. Fineberg, S. P. Gross, M. Marder, and H. L. Swinney, Instability in the propagation of fast cracks, Phys. Rev. B **45**, 5146 (1992).

[25] E. Sharon, S. P. Gross, and J. Fineberg, Energy Dissipation in Dynamic Fracture, Phys. Rev. Lett. **76**, 2117 (1996).

[26] S. Santucci, M. Grob, R. Toussaint, J. Schmittbuhl, A. Hansen, and K. J. Måløy, Fracture roughness scaling: A case study on planar cracks, Europhys. Lett. **92**, 44001 (2010).

[27] J. Schmittbuhl, A. Delaplace, and K. J. Måløy, Propagation of an interfacial crack front in a heterogeneous medium: Experimental observations, in *Physical Aspects of Fracture*, edited by E. Bouchaud, D. Jeulin, C. Prioul, and S. Roux (Springer, Dordrecht, New York, 2001), pp. 353–369.

[28] J. Schmittbuhl, A. Hansen, and G. G. Batrouni, *Roughness of Interfacial Crack Fronts: Stress-Weighted Percolation in the Damage Zone*, Phys. Rev. Lett. **90**, 045505 (2003).

[29] K. J. Måløy, S. Santucci, J. Schmittbuhl, and R. Toussaint, Local Waiting Time Fluctuations Along a Randomly Pinned Crack Front, Phys. Rev. Lett. **96**, 045501 (2006).

[30] W. G. Knauss, An observation of crack propagation in anti-plane shear, Int. J. Fract. Mech. **6**, 183 (1970).

[31] J. Schmittbuhl, A. Delaplace, K. J. Måløy, H. Perfettini, and J. P. Vilotte, Slow crack propagation and slip correlations, Pure Appl. Geophys. **160**, 961 (2003).

[32] K. T. Tallakstad, R. Toussaint, S. Santucci, J. Schmittbuhl, and K. J. Måløy, Local dynamics of a randomly pinned crack front during creep and forced propagation: An experimental study, Phys. Rev. E **83**, 046108 (2011).

[33] J. R. Rice, First-order variation in elastic fields to variation in location of a planar crack front, J. Appl. Mech. **52**, 571 (1985).

[34] F. Family and T. Vicsek, Scaling of the active zone in the eden process on percolation networks and the ballistic deposition model, J. Phys. A **18**, L75 (1985).

[35] J. Schmittbuhl, S. Roux, and Y. Berthaud, Development of roughness in crack propagation, Europhys. Lett. **28**, 585 (1994).

[36] M. Grob, J. Schmittbuhl, R. Toussaint, L. Rivera, S. Santucci, and K. J. Måløy, Quake catalogs from an optical monitoring of an interfacial crack propagation, Pure Appl. Geophys. **166**, 777 (2009).

[37] F. Sharif, M. T. Kortschot, and R. H. Martin, Mode III delamination using a split cantilever beam, in *Composite Materials: Fatigue and Fracture*, edited by R. H. Martin, Vol. 5 (ASTM, Philadelphia, 1995), pp. 85–99.

[38] H. Gao, J. R. Rice, and J. Lee, Penetration of a quasi-statically slipping crack into a seismogenic zone of heterogeneous fracture resistance, J. Geophys. Res. **96**, 21535 (1991).

[39] K. S. Gjerden, A. Stormo, and A. Hansen, Local dynamics of a randomly pinned crack front: A numerical study, Front. Phys. **2**, 66 (2014).

[40] A. Hesham, Ultrasonic pulse echo studies of the physical properties of pmma, ps, and pvc, Polymer Plast. Tech. Eng. **42**, 193 (2003).

[41] A. Delaplace, J. Schmittbuhl, and K. J. Måløy, High resolution description of a crack front in a heterogeneous Plexiglas block, Phys. Rev. E **60**, 1337 (1999).